Seismic reflector imaging using internal multiples with Marchenko-type equations

Evert Slob[1], Kees Wapenaar[1], Filippo Broggini[3], and Roel Snieder[2]

ABSTRACT

We present an imaging method that creates a map of reflection coefficients in correct one-way time with no contamination from internal multiples using purely a filtering approach. The filter is computed from the measured reflection response and does not require a background model. We demonstrate that the filter is a focusing wavefield that focuses inside a layered medium and removes all internal multiples between the surface and the focus depth. The reflection response and the focusing wavefield can then be used for retrieving virtual vertical seismic profile data, thereby redatuming the source to the focus depth. Deconvolving the upgoing by the downgoing vertical seismic profile data redatums the receiver to the focus depth and gives the desired image. We then show that, for oblique angles of incidence in horizontally layered media, the image of the same quality as for 1D waves can be constructed. This step can be followed by a linear operation to determine velocity and density as a function of depth. Numerical simulations show the method can handle finite frequency bandwidth data and the effect of tunneling through thin layers.

INTRODUCTION

From the late 1960s to the early 1980s, much work has been done on 1D exact inversion methods for scalar wave problems for applications in geophysics (Ware and Aki, 1969; Burridge, 1980; Coen, 1981). Most derivations use stretching and scaling of the wave equation to write it in a form resembling the Schrödinger equation for which the exact inversion method originally was developed (Agranovich and Marchenko, 1963; Lamb, 1980). The interest was briefly revived when Rose (2002) showed how 1D focusing

can be achieved with the Marchenko equation, and he used an iterative solution method to demonstrate it. Recently, Broggini et al. (2012) used the idea to retrieve a virtual vertical seismic profile (VSP) with the virtual source inside the layered medium at any depth location and the receivers at the surface. The virtual VSP was retrieved from surface reflection data and the method was extended to 3D data-driven redatuming (Wapenaar et al., 2012). Wapenaar et al. (2013a) derived a new Newton-Marchenko scheme in 3D to image reflectors without creating ghosts images from internal multiples. In that sense, such schemes are distinctly different from known methods that aim to remove internal multiples using the inverse scattering series (Zhang and Weglein, 2009; Weglein et al., 2012) or to predict and subtract internal multiples (Jakubowicz, 1998; ten Kroode, 2002) from the reflection data at the surface. Imaging schemes that use Marchenko-type equations focus the wavefield inside a heterogeneous medium, use the internal multiples to construct correct image amplitudes, and do not create ghost reflectors because the internal multiples are handled correctly.

Direct inversion using reflection data measured at one side of the target in 1D is possible for infinite bandwidth data, which is not available in measured seismic data. Imaging can be achieved with a limited frequency bandwidth as available from seismic data with a penalty on the achievable resolution. Similar to the work of Wapenaar et al. (2013a), our aim is to form an image using only reflection data measured at one side of the target. By investigating how downgoing and upgoing waves in a layered medium can be focused at a chosen depth level, we derive an exact imaging scheme. To create an image of only primary reflection events from measured data at the surface, it is necessary to redatum the sources and receivers to the image location. This should be done in a data-driven way. Direction is important, and we keep upgoing and downgoing waves separated.

In this paper, we follow a different route than Wapenaar et al. (2013a) by first finding out what is the incident field that creates a focus just below the bottom interface of a layered medium; we

call this the *focusing wavefield*. We then find two relations between the focusing wavefield, the surface impulse reflection response, and VSP responses for a source at the focus depth inside a layered medium. From these relations, we derive an imaging scheme and show how the image can be used to determine the medium properties and layer thickness in case waves at several oblique angles of incidence are used. With a numerical example, we investigate the effects of finite bandwidth and of tunneling waves on the performance of the imaging scheme. In Appendix A, we give a mathematical derivation of the results with the aid of the acoustic reciprocity theorems of the time-convolution and time-correlation types.

FOCUSING A WAVEFIELD JUST BELOW A LAYERED MEDIUM

This section is dedicated to finding expressions for the focusing wavefield. Later, we will investigate how we can retrieve the focusing wavefield from the measured impulse reflection response. For a normal incidence plane wave, we assume to have measured the acoustic pressure $p(z_0, t)$ below the source, but just above the first reflector, which we denote as the surface. We can describe the acoustic pressure as the sum of downgoing $p^+(z, t)$ and upgoing $p^-(z, t)$ waves as $p(z, t) = p^+(z, t) + p^-(z, t)$, where z is depth and t is time. We start with a medium containing three layers and the two interfaces separating them are located at depth levels z_0 and $z_1 > z_0$. The densities and velocities in the three layers are denoted ρ_i, c_i, with $i = 0, 1, 2$, respectively. The thickness of the second layer is given by $d_1 = z_1 - z_0$ and the corresponding one-way traveltime is denoted $t_1 = d_1/c_1$. For a downgoing pressure wave incident on an interface at depth level z_i, the local reflection and transmission coefficients are given by r_i, τ_i^+, and for an upgoing incident wave by $-r_i$, τ_i^-. The two-way transmission coefficient is given by $\tau_i^2 = \tau_i^+ \tau_i^-$. First, we send a normal incidence plane downgoing acoustic pressure wave from above and the upgoing field just above z_0 consists of an infinite number of events. The first two are primary reflections followed by a series of multiple

Figure 1. Reflection and transmission responses (a) and the focusing wavefields (b).

reflections as indicated in Figure 1a. We call the total upgoing field the *impulse reflection response* $R(z_0, t)$. The position z_0 in the argument indicates that source and receiver are at the same depth level, hence $p^-(z_0, t) = R(z_0, t)$. In the third layer, the downgoing wavefield consists of a direct arrival followed by multiples. We call this the *transmission response* $T^+(z_1, z_0, t)$, measured at z_1 and generated by the source at z_0, hence $p^+(z_1, t) = T^+(z_1, z_0, t)$. We can write these upgoing and downgoing pressure fields in the frequency domain, with radial frequency ω, as

$$\hat{p}^+(z_0, \omega) = 1, \qquad \hat{p}^-(z_0, \omega) = \frac{r_0 + r_1 \exp(-2i\omega t_1)}{1 + r_0 r_1 \exp(-2i\omega t_1)}, \tag{1}$$

$$\hat{p}^+(z_1, \omega) = \frac{\tau_0^+ \tau_1^+ \exp(-i\omega t_1)}{1 + r_0 r_1 \exp(-2i\omega t_1)}, \qquad \hat{p}^-(z_1, \omega) = 0, \tag{2}$$

where the diacritical hat denotes a quantity in frequency domain and $\hat{p}(z_0, \omega)$, $\hat{p}(z_1, \omega)$ denote the acoustic pressure just above z_0 and just below z_1. This notion is used throughout the paper. By expanding the denominator, the infinite number of events are obtained that belong to the reflection and transmission responses.

From Figure 1a, it is clear that if we are able to eliminate the second downgoing event just below the reflector at z_0, only one event reaches depth level z_1. This would constitute a focused wavefield at z_1. It is achieved by sending in a new downgoing wave with amplitude $r_0 r_1$ that reaches depth level z_0 at $t = t_1$ as indicated in Figure 1b. In the figure, all incident waves are time advanced by the one-way traveltime t_1 of the second layer such that the focus occurs at $t = 0$. Notice that, by focusing the wavefield at depth level z_1, all internal multiples have been eliminated. Another interesting feature is that the reflection response in Figure 1b has only two events and both have the correct local reflection amplitudes of the two reflectors. To create a unit amplitude focus, the inverse of the transmission response has to be sent in. We denote this downgoing focusing wavefield $f_1^+(z_0, z_1, t)$. The upgoing part is the corresponding reflection response, and we denote it $f_1^-(z_0, z_1, t)$. The argument z_1 is inserted to indicate the depth level just below which the pressure wavefield is focused. These two wavefields together form the focusing wavefield. By looking at equations 1 and 2, we can see that at z_0 the focusing wavefield can be written as

$$\hat{f}_1^+(z_0, z_1, \omega) = \frac{1}{\hat{T}^+(z_1, z_0, \omega)} = \frac{e^{i\omega t_1} + r_0 r_1 e^{-i\omega t_1}}{\tau_0^+ \tau_1^+}, \tag{3}$$

$$\hat{f}_1^-(z_0, z_1, \omega) = \frac{\hat{R}(z_0, \omega)}{\hat{T}^+(z_1, z_0, \omega)} = \frac{r_0 e^{i\omega t_1} + r_1 e^{-i\omega t_1}}{\tau_0^+ \tau_1^+}. \tag{4}$$

Because time-reversed solutions satisfy the same wave equation, we investigate the result of sending in the time-reversed reflection response $f_1^-(z_0, z_1, -t)$. This is depicted in Figure 2, where the incident wavefield is the time-reversed reflection response of Figure 1b given by $r_1\delta(t + t_1) + r_0\delta(t - t_1)$. The corresponding reflection response is also shown in Figure 2. The first event in the reflection response, $r_0 r_1 \delta(t + t_1)$, is the time-reverse of the second incident wave of the focusing wavefield. The first term in the
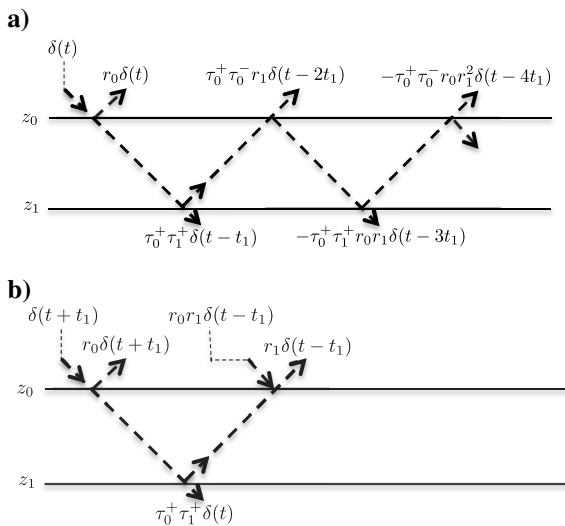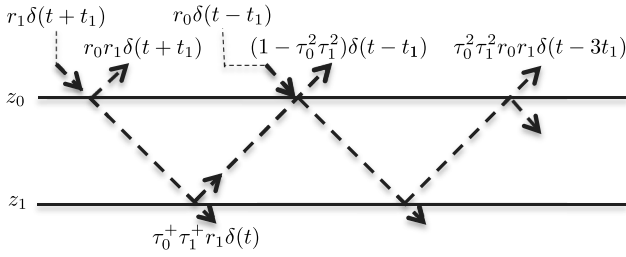
Figure 2. The time-reverse of the reflection response generated by the focusing wavefield of Figure 1b incident on the same medium.

second reflection event, $\delta(t - t_1)$ is the time-reverse of the first incident wave of the focusing wavefield. The second term, $-\tau_0^2\tau_1^2\delta(t - t_1)$, can be interpreted as minus the direct arrival from an upgoing source wavefield generated just below z_1 and received at z_0. The source strength is equal to the product of the local transmission coefficients. The third term in the reflection event, $\tau_0^2\tau_1^2 r_0 r_1\delta(t - 3t_1)$, can be interpreted as the first multiple of the transmission response of the same source at z_1 and receiver at z_0. Because all later terms will just be multiples inside the second layer, we can conclude that sending in the time-reversed reflection response of the focusing wavefield, $f_1^-(z_0, z_1, -t)$, results in a new reflection response that is equal to the time-reverse of the incident focusing wavefield, $f_1^+(z_0, z_1, -t)$, minus the pressure field Green's function $G^{p,-}(z_0, z_1, t)$ that belongs to an upgoing source at z_1 and pressure field receiver at z_0. In the frequency domain, we can express this as

$$[\hat{f}_1^+(z_0, z_1, \omega)]^* - \hat{G}^{p,-}(z_0, z_1, \omega)$$
$$= R(z_0, \omega)[\hat{f}_1^-(z_0, z_1, \omega)]^*, \tag{5}$$

and equation 5 can be interpreted as a VSP-type Green's function expression in terms of the focusing wavefield and the impulse reflection response. The fact that this is only for the upgoing part of the source wavefield is indicated by the minus-sign in the superscript with the Green's function. The superscript p indicates that it is the pressure field. Notice that, in the time domain, the focusing wavefield and the Green's function in the left-hand side of equation 5 are nonzero in mutually exclusive time windows except for the overlapping time instant $t = t_1$ of the first arrival of the Green's function and the last arrival of the time-reversed downgoing focusing wavefield (see Figure 2).

The above focusing result can be used for any number of interfaces in the 1D model. In the frequency domain, the reflection and transmission responses for any layered medium can be written in the fractional form used above and their denominators are always the same (Goupillaud, 1961). This means that the focusing wavefield for a medium with interfaces from z_0 to z_i can be written as

$$\hat{f}_1^+(z_0, z_i, \omega) = [\hat{T}^+(z_i, z_0, \omega)]^{-1}, \tag{6}$$

$$\hat{f}_1^-(z_0, z_i, \omega) = \hat{R}(z_0, \omega)/\hat{T}^+(z_i, z_0, \omega), \tag{7}$$

$$\hat{f}_1^+(z_i, z_i, \omega) = 1, \tag{8}$$

$$\hat{f}_1^-(z_i, z_i, \omega) = 0. \tag{9}$$

As an example, we extend the model with a third interface at z_2, with $z_2 > z_1$. Figure 3 shows seismic pressure reflection responses to a layered medium with the values for the velocities and densities of the first four layers in Table 1. In this model, density contrasts are stronger than velocity contrasts. In the figure, $z_0 = 75$ m means that the source and receiver are 75 m above the first interface, $z_1 = 192$ m, and $z_2 = 291$ m. The interfaces are indicated in the plots by horizontal black lines. For all plots, $t = 0$ is chosen such that it coincides with first arrival at z_2, which is the depth level where we want to focus the wavefield. Figure 3a shows the acoustic pressure in this layered medium for a single incident pressure wave. Figure 3b shows the response for an impulse followed by a second incident wave. In this case, the upward traveling reflection from z_1 arrives at z_0 at the same moment the new incident waves arrives at z_0 and together they create only an upgoing wave. At this moment, the wavefield is focused at depth level z_1 as in the first example, but because the focused wave continues to travel downward it creates new reflections from the interface at z_2 and those waves interact with all the interfaces. Figure 3c shows the same as 3b, but now with a third incident wave that is taken such that it arrives at z_1 at the same moment that the upcoming reflection from z_2 arrives at z_1 and again such that no downgoing wave is created at z_1. This third incident wave creates an extra reflection at z_0, which has very small amplitude and is barely visible in the plot. Figure 3d shows the final result where the wavefield is focused at z_2 and a fourth incident wave is taken such that it arrives at z_0 at the moment that the upgoing reflected wave from z_2 arrives at z_0. The incident wave is again such that no downgoing wave at z_0 is created. Now the wavefield is focused at z_2 and no other events occur at that depth level. The mathematical details of the waves shown in Figure 3d are given in Appendix A.

It can be seen from Figure 3 that, to focus the wavefield at the bottom reflector, a finite number of waves have to be sent in from the first layer. Comparing this result with the result from the previous example with two interfaces shows that, to focus the wavefield at the bottom reflector, the number of waves we need to send into a layered medium is doubled for every reflector that is added. The corresponding reflection response has the same number of waves. If we replace z_1 by z_i in equation 5, the equation is still valid. We conclude that this is a valid equation for an arbitrarily layered model and a general derivation is given in Appendix A.

Now we know what the focusing wavefield looks like. The downgoing focusing wavefield incident on a layered medium with interfaces from z_0 to the focus depth z_i has 2^i waves and the reflection response has the same number of waves. At the level z_0, the focusing wavefield exists in the time domain between $-t_d(z_i, z_0) \leq t \leq t_d(z_i, z_0)$, $t_d(z_i, z_0) = \sum_{n=1}^{i} d_n/c_n$ being the one-way traveltime across the layered medium. We also know that, at the focus time, the upgoing part at the receiver level contains the local reflection coefficient r_i scaled by the product of local transmission coefficients. This will be useful for imaging if we are able to make three more steps. First, we should be able to use this focusing wavefield to focus inside a layered medium. Second, we must find the way to determine this focusing field from the measured reflection data, and as third step we must formulate an imaging scheme. Each step is carried out in the three subsequent sections.
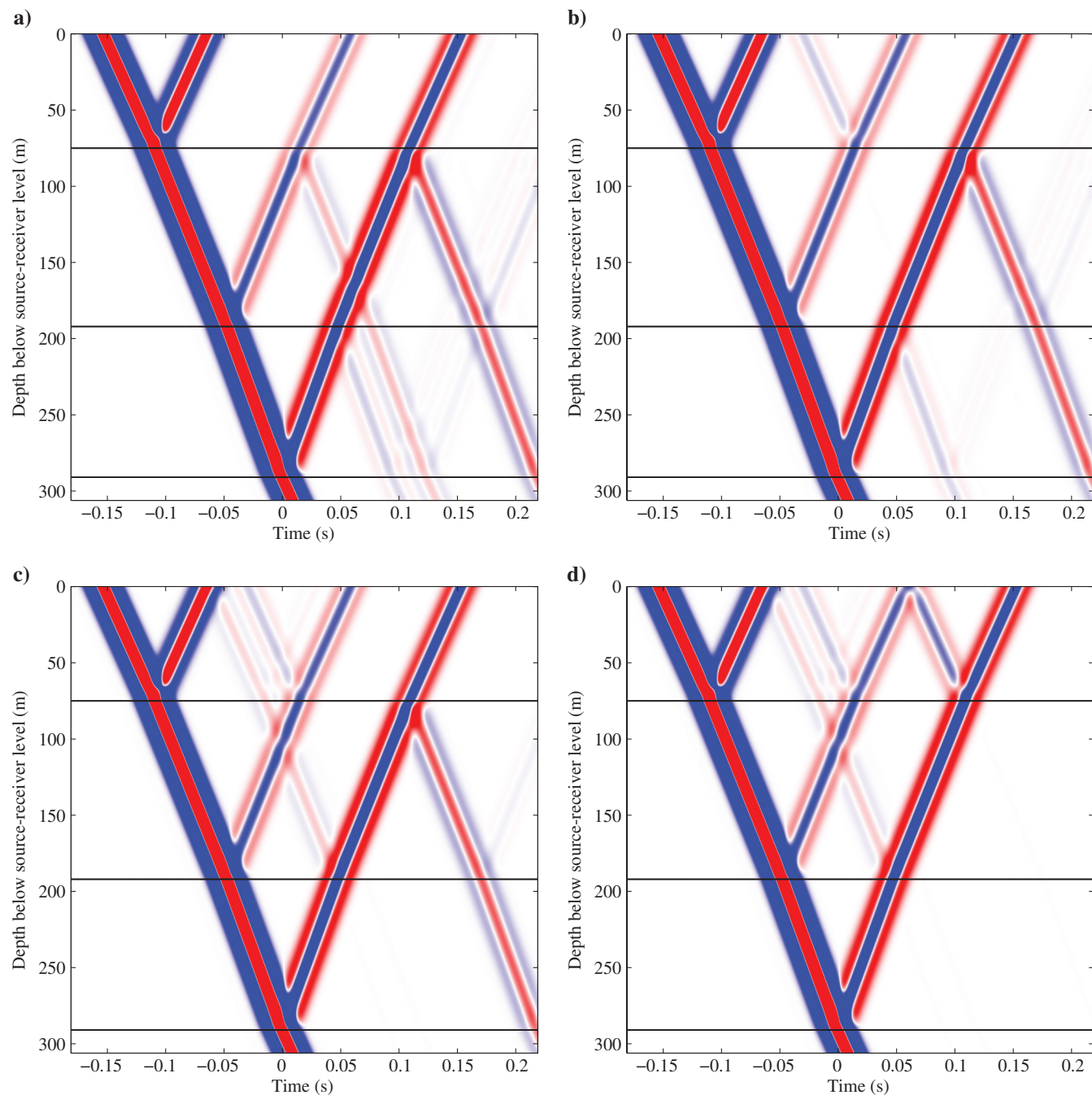
Slob et al.

a)

b)

c)

d)

Figure 3. (a) The impulse reflection response of a four-layered medium where the layer boundaries inside the plot are indicated by three black horizontal lines labeled on the right side by z_0, z_1, z_2, (b) the reflection response of (a) but now with an extra incident wave that cancels the downgoing field at the first interface; (c) the reflection response of (b) but now with an extra incident wave that cancels the downgoing wave at the second interface; (d) the reflection response of (c) but now with an extra incident wave that cancels the downgoing wave at the first interface generated by the reflected wave from the bottom interface.

FOCUSING THE WAVEFIELD INSIDE A LAYERED MEDUM

We extend the layered model further by introducing an arbitrary number of reflectors below z_i, but use z_i as focus depth. Figure 4 shows the situation with four downgoing arrows at z_0 indicating waves that are sent into the medium and four solid upgoing arrows

indicating the reflection response. The wavefield focuses at z_i at $t = 0$, but because the focusing wavefield continues to travel down, it will generate new up- and downgoing waves indicated by the dashed arrows in Figure 4. These waves arrive at z_0 after the last arrival of the focusing wavefield. They all start as a unit amplitude downgoing wave just below z_i as if there was a downgoing source just below z_i, and hence all waves that are generated and recorded at

z_0 correspond to part of a VSP measurement that is complementary to what we saw in the previous section. In the frequency domain, this pressure Green's function can be written as $\hat{G}^{p,+}(z_0, z_i, \omega)$ and it corresponds to the events indicated by the dashed lines in Figure 4, whereas the focusing wavefield corresponds to the solid lines. The impulse reflection response, $\hat{R}(z_0, \omega)$, generated by a downgoing unit amplitude pressure wavefield and measured at z_0 in the whole layered medium is related to the focusing wavefield and the downgoing Green's function by (see Appendix A for general derivation)

$$\hat{f}_1^-(z_0, z_i, \omega) + \hat{G}^{p,+}(z_0, z_i, \omega) = \hat{R}(z_0, \omega)\hat{f}_1^+(z_0, z_i, \omega). \tag{10}$$

Equation 10 is the wavefield retrieval equation for the wavefield generated by a downgoing source at z_i and received at z_0. It is obtained from the measured impulse reflection response and the functions $\hat{f}_1^\pm$. This equation can be interpreted as follows. If the wavefield $f_1^+(z_0, z_i, t)$ is sent into the layered medium, the reflection response at z_0 is given by $R(z_0, t) * f_1^+(z_0, z_i, t)$ where the $*$ denotes temporal convolution. Equation 10 says that this response is equal to $f_1^-(z_0, z_i, t)$ plus the Green's function $G^{p,+}(z_0, z_i, t)$ corresponding to a downgoing source at the focusing level and a pressure receiver at the original receiver level. This is illustrated in Figure 5 where the model consists of seven layers and the values for velocity, density, and layer thickness are taken from Table 1. The source and receiver are at 75 m above z_0. The depth levels of the interfaces are indicated by black lines in the figure. The focusing time is again $t = 0$ at the moment where the first arrival reaches the focus depth $z_2 = 291$ m. From the figure, it can be seen that $f_1^\pm(z_0, z_i, t)$ and $G^{p,+}(z_0, z_i, t)$ are well-separated in time as indicated above the figure. Equation 5 is also valid when the focusing depth level is inside a layered medium,
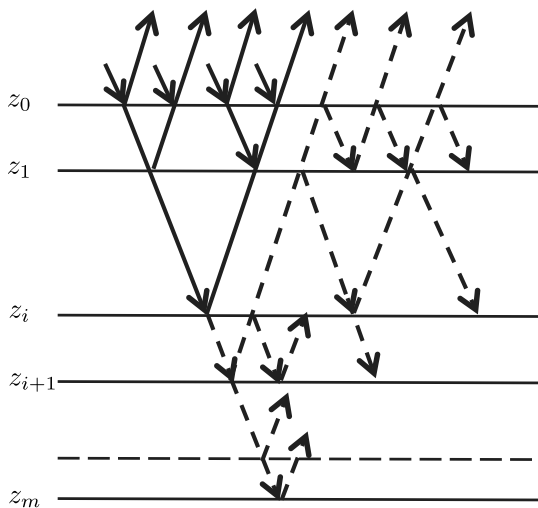

Figure 4. The focusing wavefield incident on a medium with $m + 2$ layers that focuses at z_i yields a reflection response that is equal to the focusing field reflection response, as indicated by the solid arrows, followed by the Green's function for a downgoing source at z_i indicated by dashed arrows.

$$[\hat{f}_1^+(z_0, z_i, \omega)]^* - \hat{G}^{p,-}(z_0, z_i, \omega) = \hat{R}(z_0, \omega)[\hat{f}_1^-(z_0, z_i, \omega)]^*. \tag{11}$$

In equation 5, the Green's function is the transmission response of a layered medium with a source below and a receiver above a layered medium. Equation 11 retrieves the wavefield $\hat{G}^{p,-}(z_0, z_i, \omega)$ at receiver level z_0 that is generated by an upgoing plane wave at the source level z_i inside the layered medium, from the measured impulse reflection response $\hat{R}(z_0, \omega)$ and the functions $\hat{f}_1^\pm$. This equation says that the convolution of the time-reversed upgoing focusing wavefield and the impulse reflection response is equal to the time-reversed downgoing focusing wavefield minus the Green's function for an upgoing source just below z_i and the pressure receiver just above z_0. It is illustrated in Figure 6 for the same configuration and focus depth as used for Figure 5. In this figure, events that belong to the focusing wavefield are indicated above the figure as $f_1^-(z_0, z_i, -t) + f_1^+(z_0, z_i, -t)$. In this wavefield, there are no up-down reflections. The only up-down reflections occurring in the time window of the focusing wavefield come from the upgoing wavefield after reflection at the boundary at z_2 as indicated by the arrows. This is part of the Green's function as indicated above the figure with $G^{p,-}$. Because the upgoing part of the Green's function is emitted at $t = 0$, which is the focusing time-instant for the focusing wavefield, they overlap along the direct travel path from the focus depth to the surface as indicated above the figure. For the rest, the focusing wavefield and the Green's functions are separated in time. In the next section, we show that the focusing wavefield can be computed from the measured reflection data and equations 10 and 11. From these, virtual VSP data and a subsurface image can be constructed as is shown in the next two sections. Knowing the up- and downgoing Green's function is important because they are related to the impulse reflection response at the focus level through

$$\hat{G}^{-,q}(z_i, z_0, \omega) = \hat{R}(z_i, \omega)\hat{G}^{+,q}(z_i, z_0, \omega), \tag{12}$$

where $\hat{R}(z_i, \omega)$ denotes the impulse reflection response for the medium that is layered below z_i and homogeneous above that depth level. The Green's functions are the reciprocal version of the ones in

Table 1. Values for velocity, density, and layer thickness in the layered model.

Layer number	Velocity (m/s)	Density (kg/m³)	Thickness (m)
1	1700	1430	∞
2	1900	2250	117
3	2100	1750	99
4	1700	1430	85
5	2100	1750	111
6	3250	1930	15
7	2100	1500	123
8	2100	2110	151
9	2500	2110	163
10	2750	2250	221
11	2900	2300	∞

equations 10 and 11. Here, the sign in the superscripts refers to the direction of the wavefield at the receiver level z_i and the superscript q refers to a monopole point source at the source level z_0. The local reflection coefficient r_i can be extracted in the time domain from $R(z_i, t)$ around $t = 0$.
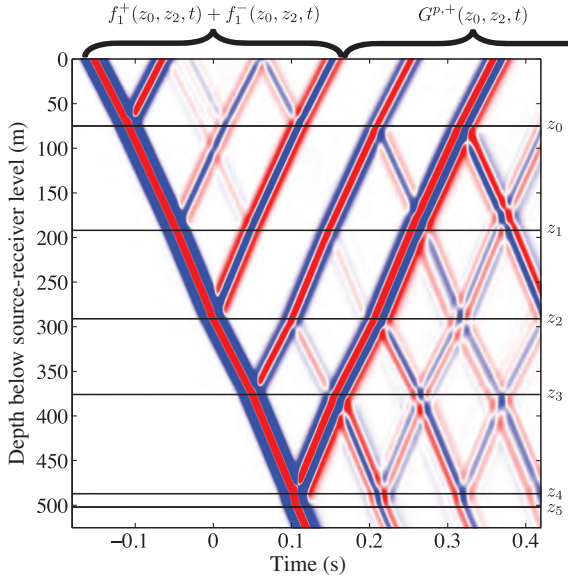

Figure 5. The wavefield incident on a medium with six interfaces, indicated with black lines, that focuses at the third interface and its reflection response; the downgoing wavefield below the third interface propagates down and causes reflections from the medium below it that interact with the whole medium.
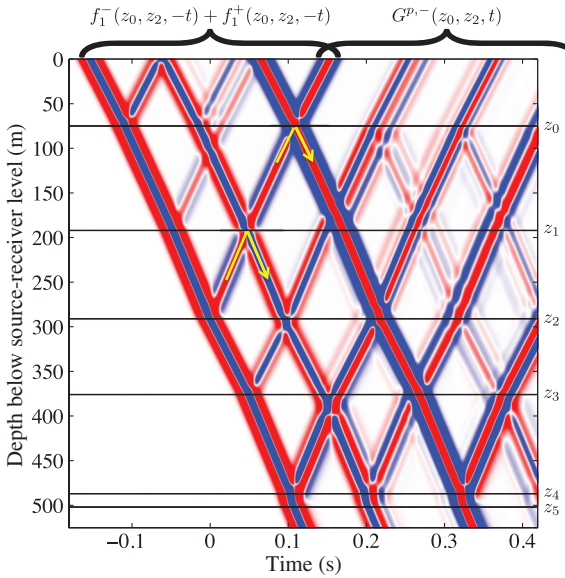

Figure 6. The time-reverse of the reflected focusing wavefield incident on a medium with six interfaces, indicated with black lines; the first arrival of the upgoing Green's function coincides with the last upgoing wave of the time-reversed downgoing focusing wavefield because both are generated simultaneously at the third interface. In the overlapping time window with the focusing wavefield, the upgoing Green's function wavefield causes up-down reflections as indicated by the arrows.

COUPLED MARCHENKO-TYPE EQUATIONS AND GREEN'S FUNCTION RETRIEVAL

The time-domain functions $f_1^{\pm}$ are not causal, whereas $G^{\pm}$ and R are. This can be exploited to find $f_1^{\pm}$ from the time-domain equivalents of equations 10 and 11. Two coupled Marchenko-type equations are obtained in which $G^{\pm}$ do not occur and from which $f_1^{\pm}$ can be found given the measured impulse reflection response $R(z_0, t)$. Once $f_1^{\pm}$ are found, time-domain versions of equations 10 and 11 can be used to compute the up- and downgoing wavefields generated by a downhole source and measured at the surface. Hence, for any depth z_i, we can create a virtual VSP data set from the measured impulse reflection response (Newton, 1981; Broggini and Snieder, 2012; Wapenaar et al., 2012).

Transforming equations 10 and 11 to the time domain results in

$$G^{p,+}(z_0, z_i, t) = -f_1^-(z_0, z_i, t)$$
$$+ \int_{t'=-t_d(z_i, z_0)}^{t} f_1^+(z_0, z_i, t') R(z_0, t - t') dt', \quad (13)$$

$$G^{p,-}(z_0, z_i, t) = f_1^+(z_0, z_i, -t)$$
$$- \int_{t'=-t_d(z_i, z_0)}^{t} f_1^-(z_0, z_i, -t') R(z_0, t - t') dt'. \quad (14)$$

The integration intervals of equations 13 and 14 are finite because the two functions in the integrands are nonzero only in a subinterval. The impulse reflection response $R(z_0, t - t')$ is causal and therefore zero-valued for $t' > t$, putting the upper limits at $t' = t$. In the previous section, we have seen that $f_1^{\pm}(z_0, z_i, t) = 0$ for $|t| > t_d(z_i, z_0)$ because all internal multiples are eliminated between the depth levels z_0 and z_i and this defines the lower integration limit of equations 13 and 14. We can write the downgoing wavefield as

$$f_1^+(z_0, z_i, t) = \mathcal{T}_i^{-1} \delta(t + t_d(z_i, z_0)) + M^+(z_0, z_i, t), \quad (15)$$

where in our 1D model the first arrival of the transmission response has amplitude $\mathcal{T}_i = \prod_{j=0}^{i} \tau_j^+$ and $M^+(z_0, z_i, t)$ denotes the coda following the first arrival; $M^+(z_0, z_i, t) = 0$ for $t \le -t_d(z_i, z_0)$. Because $M^+(z_0, z_i, t) = 0$ and $f_1^-(z_0, z_i, t) = 0$ for $|t| \ge t_d(z_i, z_0)$ and $G^{\pm} = 0$ for $t < t_d(z_i, z_0)$, we can write in the interval $-t_d(z_i, z_0) < t < t_d(z_i, z_0)$ equations 13 and 14 as two coupled equations as

$$f_1^-(z_0, z_i, t) = \mathcal{T}_i^{-1} R(z_0, t + t_d(z_i, z_0))$$
$$+ \int_{t'=-t_d(z_i, z_0)}^{t} M^+(z_0, z_i, t') R(z_0, t - t') dt', \quad (16)$$

$$M^+(z_0, z_i, -t) = \int_{t'=-t_d(z_i, z_0)}^{t} f_1^-(z_0, z_i, -t') R(z_0, t - t') dt', \quad (17)$$

which are coupled Marchenko-type equations (Lamb, 1980) valid on the interval $-t_d(z_i, z_0) < t < t_d(z_i, z_0)$. These can be solved for the functions $M^+(z_0, z_i, t)$ and $f_1^-(z_0, z_i, t)$ from the measured impulse reflection response $R(z_0, t)$ when the amplitude of the first arrival of the transmission response, $\mathcal{T}_i$, is known. A straightforward way to solve equations 16 and 17 is to discretize them and solve the resulting matrix inversion problem. We can also solve the coupled system with an iterative procedure and start by taking

$$f_{1;0}^-(z_0, z_i, t) = \mathcal{T}_i^{-1} R(z_0, t + t_d(z_i, z_0)), \tag{18}$$

and for $n \geq 0$ evaluate the nth iteration as

$$M_n^+(z_0, z_i, -t) = \int_{t'=-t_d(z_i,z_0)}^{t} f_{1;n}^-(z_0, z_i, -t') R(z_0, t - t') dt', \tag{19}$$

$$f_{1;n+1}^-(z_0, z_i, t) = f_{1;0}^-(z_0, z_i, t) \\ + \int_{t'=-t_d(z_i,z_0)}^{t} M_n^+(z_0, z_i, t') R(z_0, t - t') dt', \tag{20}$$

for $-t_d(z_i, z_0) < t < t_d(z_i, z_0)$. This scheme always converges because the underlying Neumann series expansion of the Green's function integral equation converges unconditionally (Lamb, 1980). Solving equations 16 and 17 using an iterative scheme is not necessary, but will often prove computationally advantageous. Once the functions $f_1^\pm(z_0, z_i, t)$ are found in their time window, equations 13 and 14 can be used to compute the Green's functions and thereby the virtual VSP is retrieved. The image can be constructed from the VSP Green's functions using equation 12. In the next section, we first find a more direct route to the image.

IMAGING

To use equations 16 and 17 for imaging, we observe that our initial estimate of the scaled delta function is always correct in arrival time because in a 1D model it is half the two-way traveltime. But, the amplitude $\mathcal{T}_i$ is not known, nor the actual depth level z_i. The 1D image can therefore be constructed as a time image when there is no additional information on the layered medium. We can scale the downgoing coda and the upgoing wavefield by the same factor $\mathcal{T}_i^{-1}$,

$$M^+(z_0, z_i, t) = \mathcal{T}_i^{-1} h^+(z_0, z_i, t), \tag{21}$$

$$f_1^-(z_0, z_i, t) = \mathcal{T}_i^{-1} h^-(z_0, z_i, t). \tag{22}$$

Using these definitions in equations 16 and 17 we find a scheme in which the unknown factor $\mathcal{T}_i$ is absent. Figure 1b shows the solution to equations 16 and 17 with substitution of equations 21 and 22 for our example model with three layers. The example showed that sending a unit amplitude impulse in time at $-t_d(z_1, z_0)$ and the coda of the scaled downgoing focusing wavefield leads to a reflected signal at $t_d(z_1, z_0)$, with the desired local reflection coefficient r_1 of the interface at depth level z_1. These scaled downgoing and upgoing wavefields can be recognized from equations 20 and 22 as $h^+(z_0, z_1, t)$ and $h^-(z_0, 6z_1, t)$. By evaluating the

time-domain equivalent of equation 10 we find that $h^-(z_0, z_i, t) = r_i \delta(t - t_d(z_i, z_0))$ for $t_d(z_i, z_0) - \epsilon < t < t_d(z_i, z_0) + \epsilon$, where ϵ is an arbitrarily small time instant. Hence, for an arbitrary depth level z_i inside a layered medium, the upgoing field that arrives at $t = t_d(z_i, z_0)$ has an amplitude that is equal to the local reflection coefficient of depth level z_i, and $t_d(z_i, z_0)$ is the known one-way traveltime to depth level z_i. We can therefore take the amplitude of the upgoing field at the focus time as the imaging condition to obtain an image $\mathcal{I}$ containing the local reflection coefficient at the one-way traveltime

$$\mathcal{I}(t_d(z_i, z_0)) = r_i = \int_{t'=t_d(z_i,z_0)-\epsilon}^{t_d(z_i,z_0)+\epsilon} h^-(z_0, z_i, t') dt'. \tag{23}$$

Equations 16 and 17 with substitution of equations 21 and 22 together form the imaging scheme and equation 23 is the imaging condition. This is the most direct route to imaging local primary reflection coefficients and simultaneously eliminating effects from internal multiples. We have not used any knowledge of the layered medium, but we have constructed an image containing the local reflection coefficient as a function of one-way traveltime. In case the acoustic impedance is known in the first layer, the impedance could be found as a function of one-way traveltime. With one-dimensional waves at normal incidence, there are no independent ways to determine a velocity model. This can be done by using several angles of incidence for plane waves, which is discussed in the next section.

PLANE WAVES AT OBLIQUE INCIDENCE

The above results for normal incidence plane waves rely on the fact that the local refection coefficients are independent of frequency. To include oblique angles, a spatial Fourier transformation can be performed on measured data yielding the impulse reflection response in the wave number frequency domain. Newton (1981) used the wave number domain where the wave numbers are just parameters, but then the reflection coefficients become frequency-dependent. He therefore continued with the assumption that the wave numbers are small and can be neglected. Coen (1981) showed that, in the intercept-time slowness domain, slowness is just a parameter representative of the angle of incidence. He had to exclude waves that are evanescent between the depth levels z_0 and z_i. In our case, this assumption is not necessary. We assume that the waves propagate through the two boundaries at z_0 and at z_i, but they can be evanescent at other depth levels. Only radial slowness p matters, and the local reflection coefficient becomes a function of slowness, denoted $r_i(p)$. The depth level z_i is still unknown, but the intercept-time is the apparent two-way vertical traveltime as a function of angle and we need the one-way intercept time as the image time. For depth level z_i, we denote the one-way intercept time as $t_d(z_i, z_0, p)$. If we define the vertical slowness in layer n as $q_n = \sqrt{1/c_n^2 - p^2}$, the intercept time is given by $t_d(z_i, z_0, p) = \sum_{n=1}^{i} q_n(z_n - z_{n-1})$. We can write equations 16 and 17 with substitution of equations 21 and 22 as

$$h^-(z_0, z_i, t, p) = R(z_0, t + t_d(z_i, z_0, p), p) \\ + \int_{t'=-t_d(z_i,z_0,p)}^{t} h^+(z_0, z_i, t', p) R(z_0, t - t', p) dt', \tag{24}$$

$$h^+(z_0, z_i, -t, p) = \int_{t'=-t_d(z_i, z_0, p)}^{t} h^-(z_0, z_i, -t', p) R(z_0, t-t', p) dt',$$

$$(25)$$

valid for $-t_d(z_i, z_0, p) < t < t_d(z_i, z_0, p)$. This leads to the angle-dependent imaging condition similar to equation 23,

$$\mathcal{I}(t_d(z_i, z_0, p), p) = r_i(p)$$
$$= \int_{t'=t_d(z_i, z_0, p)-\epsilon}^{t_d(z_i, z_0, p)+\epsilon} h^-(z_0, z_i, t', p) dt'.$$

$$(26)$$

The image $\mathcal{I}$ is an image in the intercept-time slowness, or τ-p, domain. For every slowness value, the image contains the local reflection coefficients at the corresponding one-way intercept times that we can call *image times*. Therefore, the image is an image gather that can be understood as a "prestack" time image, where prestack should be understood in the slowness-domain and each time is the correct one-way traveltime corresponding to a particular slowness value. Having slowness as a free parameter implies that the local reflection coefficients in the image can be converted to velocity and density values in each layer. This would constitute an inversion step and after the velocities are found, the image times can be converted to depth. Much work has been carried out on AVA inversion (e.g., Raz, 1981), but here we have two advantages. The first is that no multiples are part of the image and we can construct local reflection coefficients as a function of angle without needing any subsurface information. The second is that we have a nonrecursive scheme and therefore no error accumulation with increasing imaging depth. Imaging followed by inversion assumes that the medium is horizontally layered and that the reflection response can be obtained from the data, which requires knowledge of the source signature, density, and velocity in the source layer, and removal of free-surface related multiples (Verschuur et al., 1992; van Dedem and Verschuur, 2005).

Finite frequency bandwidth

The above algorithm is formulated with impulse response functions, which we don't have in seismic data. For measured signals, we need to deal with the finite frequency bandwidth of the data. Let the finite bandwidth be represented by a zero-phase filter function, or wavelet $W(t)$, in the time domain, the functions $\bar{f}_1^{\pm}$ and the measured reflection response $\bar{R}$ can be written as the time convolution of the functions $f_1^{\pm}$ and R as

$$\bar{f}_1^{\pm}(z_0, z_i, t, p) = \int_{t'=-t_d(z_i, z_0, p)}^{t_d(z_i, z_0, p)} f_1^{\pm}(z_0, z_i, t', p) W(t-t') dt',$$

$$(27)$$

$$\bar{R}(z_0, t, p) = \int_{t'=0}^{t+t_w} R(z_0, t', p) W(t-t') dt', \quad (28)$$

where $\bar{f}_1^{\pm}(z_0, z_i, t, p) = 0$ for $|t| > t_d^+$, $t_d^+ = t_d(z_i, z_0, p) + t_w$, and t_w denotes the half time window of the wavelet, while $\bar{R} \neq 0$ for $t > -t_w$. Now, a time window has to be chosen instead of a single time instant for the arrival time of the first arrival. We have to take into account the finite bandwidth versions of equations 13 and 14 and we must use a smaller time window in which the band-limited

Green's functions are zero, $\bar{G}^+(z_i, z_0, t, p) = 0$ for $t < t_d^-$ with $t_d^- = t_d(z_i, z_0) - t_w$ and $\bar{G}(z_i, z_0, t, p) = 0$ for $t \leq t_d^-$. Then equations 16 and 17 can be written as

$$\bar{f}_1^-(z_0, z_i, t, p) = \bar{f}_{1;0}^-(z_0, z_0, t, p)$$
$$+ \int_{t'=-t_d^-}^{t} \bar{M}^+(z_0, z_i, t', p) R(z_0, t-t', p) dt',$$

$$(29)$$

$$\bar{M}^+(z_0, z_i, -t, p)$$
$$= \int_{t'=-t_d^-}^{t} \bar{f}_1^-(z_0, z_i, -t', p) R(z_0, t-t', p) dt', \quad (30)$$

for $t < t_d^-$ because the Green's functions have to be zero, but $\bar{f}^{\pm}$ exist up to $t = \pm(t_d(z_i, z_0, p) + t_w)$. In the time window $-t_d^+ < t < -t_d^-$, the functions $\bar{M}^+(z_i, z_0, -t, p)$ and $\bar{f}_1^-(z_i, z_0, t, p)$ cannot be updated because they overlap with the Green's functions that should remain zero for equations 29 and 30 to be valid. Waves that have propagated or tunneled through thin layers and whose multiples arrive within the time window of the wavelet around t_d should be incorporated in $\bar{f}_{1;0}^-(z_i, z_0, t, p)$. Equation 18 should then be modified to include a more general function $\mathcal{T}_d^{-1}$,

$$\bar{f}_{1;0}^-(z_0, z_i, t, p) = \int_{t'=-t_d^+}^{-t_d^-} \mathcal{T}_d^{-1}(z_i, z_0, t', p) R(z_0, t-t', p) dt',$$

$$(31)$$

in which $\mathcal{T}_d^{-1}$ denotes the band-limited version of the first arrival in the inverse transmission response of the medium that is layered between z_0 and z_i. Notice that information from below z_i can leak into $\mathcal{T}_d^{-1}$ when there is a reflector close to but below z_i. In that case, it will lead to errors in imaging thin layers and it is part of the resolution problem associated with finite bandwidth data. Finally, from the fact that $\bar{R}$ is known from the data while R occurs in equations 29 and 30 we observe that the wavelet W should be known. In case the free-surface multiples are removed by a surface-related multiple removal method, the source signature is often obtained as well, which can then be made zero phase and used as the wavelet. In case the reflection response is obtained through up-down decomposition and deconvolution (van der Neut et al., 2011), the band-limited impulse response is obtained and a desired shaping filter can be used. The bandwidth and associated effects of thin layers are investigated in the section with numerical examples.

When thin layer effects are absent, the band-limited versions of equations 24 and 25 will produce an accurate image from equation 26. In case thin layer effects are severe, we have an alternative for creating the image. We can compute the upgoing and downgoing Green's functions. We can use the fact that the Green's functions are related through the reflection response $\bar{R}(z_i, t', p)$ of the medium that is layered below z_i and homogeneous above z_i. We can therefore write them in a similar form as equation 12, given by

$$\bar{G}^{-,q}(z_i, z_0, t, p) = \int_{t'=0}^{t} R(z_i, t-t', p) \bar{G}^{+,q}(z_i, z_0, t', p) dt'.$$

$$(32)$$

From this equation, $R(z_i, t, p)$ is found by deconvolution and the image can be constructed. Another option is to pick a time above a

reflection event, compute the reflection response, and image the first reflector using inverse wavefield extrapolation. As a direct consequence of our development here, we can state that a reflector at depth level z_i can be imaged using this scheme when the waves propagate through this depth level, while they are allowed to be evanescent between z_0 and z_i. It can be understood that signal-to-noise ratios will determine the accuracy of such images, but in principle our schemes can image interfaces below thin high-velocity layers through which the waves have tunneled. We show a numerical example later, but we can already understand from the above scheme that when $\mathcal{T}_d$ contains information on tunneling waves, it can be important to have an accurate time-function estimate of $\mathcal{T}_d^{-1}$ because it is not updated. This can lead to small errors in M^+ and f_1^- that are not eliminated by the deconvolution procedure for imaging.

NUMERICAL EXAMPLES

For the examples, we take a medium with 11 layers separated by 10 interfaces. The velocities, densities, and thicknesses of the layers are given in Table 1. The reflection data is computed in the frequency-slowness domain for 36 slowness values corresponding to for 36 angles of incidence from normal incidence to $\alpha = 35°$. The data are computed using a reflectivity code and are then transformed to the intercept-time slowness domain with source and receivers at the same height of 75 m above the top interface. This is equivalent to modeling a single shot gather in space-time and then transforming the data to the τ-p domain. The source signature is a 40-Hz Ricker wavelet. The sixth layer is a high-velocity thin layer. The seventh and eight layers have no velocity contrast and the reflection coefficient of that interface is independent of incidence angle. The eighth and ninth layers have no density contrast. The incidence angle of 31.6° in the first layer becomes critical in the high-velocity thin layer, which amounts to a critical angle of 40.25° at the top of the thin layer. At normal incidence, the fast thin layer is just over one fifth of the wavelength at 40 Hz. We solve equations 29 and 30 for each of the 36 angles of incidence using the iterative scheme similar to the one described in equations 19 and 20 in which we use $p = \sin(\alpha)/c_0$, c_0 being the velocity in the first layer. We use two different schemes solving equations 29 and 30. First, we use the direct imaging method using the initial estimate of equations 18, 21, and 22, all three extended as functions of p, in combination with imaging condition of equation 26. Second, we use the imaging by multidimensional deconvolution method, which requires an initial estimate given by equation 31. Once the $f_1^\pm$ functions are determined, the Green's functions are computed using equations 13 and 14, both extended as functions of p, from which the reflection response is computed using equation 32 and the image is constructed by standard wavefield extrapolation and imaging. Angles reported in results and figures below refer to the incidence angle in the first layer.

Imaging directly using equation 26

We solve equations 29 and 30, but the first term in the right-hand side of equation 29 is replaced by $\bar{R}(z_0, t + t_d(z_i, z_0, p))$ and we use equations 21 and 22, extended as functions of p, in combination with the imaging condition of equation 26. The iterations stop when

$$\sqrt{\sum_m (\bar{f}_{1;n}(z_0, z_i, m\Delta t, p) - \bar{f}_{1;n-1}(z_0, z_i, m\Delta t, p))^2}$$
$$\leq \sqrt{\sum_m (\bar{f}_{1;n}(z_0, z_i, m\Delta t, p))^2}/1000, \qquad (33)$$

in which n is the iteration number and the discrete time steps are given by $t = m\Delta t$, Δt being the time step. For angles up to 25°, the average number of iterations slowly rises from eight at normal incidence to 11 at 25°, between 26° and 31° the number of iterations rises from 12 to 17, and the scheme needs 21, 24, 28, and 31 iterations for the last four angles where the first is just below and the last three are beyond the critical angle for the high-velocity thin layer. The data and the resulting image are shown in the intercept time-slowness domain where slowness has been converted to incidence angle in Figures 7 and 8. Figure 7 shows that it is hard to discriminate multiples from primary reflections from 0.5 s onward. In Figure 8, the expected model reflection coefficients are shown in black solid lines and the image amplitudes are shown in red dashed lines. From the figure, it can be seen that all multiple energy has been eliminated while all primary reflections are imaged to their image times. The amplitudes and wave shapes of the first four reflectors are constructed almost exactly. For later reflectors, two types of errors occur. For all these arrivals, the phase changes due to thin layer effects because multiples arrive within the time window of the Ricker wavelet. Tunneling effects of waves transmitted through the fast thin layer are visible in the last three traces.

To see the effect of the thin layer and of tunneling, we zoom in and take a look at the image results of the first and last traces from these data. Figure 9 shows the normal incidence image as a function of image time. To create this image, only the solutions to equations 29 and 30 are computed, which requires no information other than the earth reflection response and the wavelet. We observe that the image inside the fast thin layer is quite accurate although the amplitude has a very small error, which can only be seen when the image is enlarged. The images of the last four interfaces show some phase changes in the wavelet and the maximum amplitude is not entirely correct. This is caused by the fact that in this scheme the initial estimate is a scaled and band limited delta-function, which ignores thin layer multiples overlapping with the first arrival. This is an effect of the finite bandwidth and is a resolution issue. Still, the
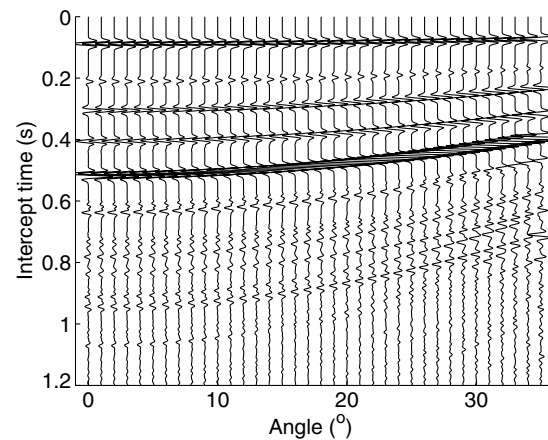

Figure 7. Reflection response data in the τ-p domain as a function of two-way intercept time and incidence angle in the first layer.

amplitudes of the last four reflectors are quite accurate and we would need to zoom in much further to make the errors visible. The obtained reflection coefficient of the eighth interface, e.g., has an amplitude error of just over 1% and zero timing error.

Figure 10 shows the image from the data with a plane wave at 35° incidence. For this angle of incidence, the waves tunnel through the
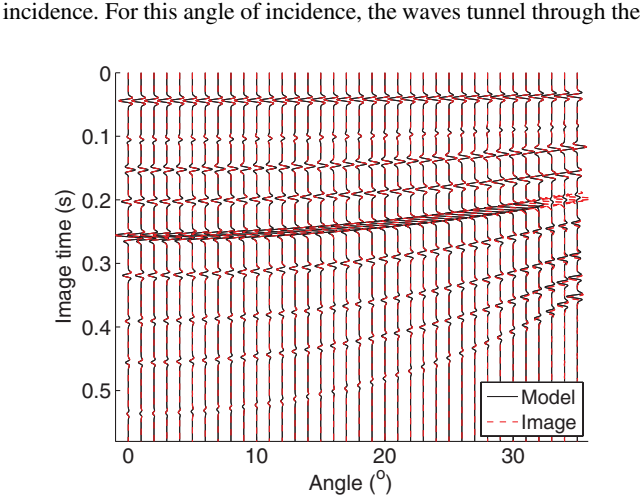

Figure 8. The image obtained as a function of one-way intercept time and angle from the data shown in Figure 7.

Figure 9. Normal incidence image.
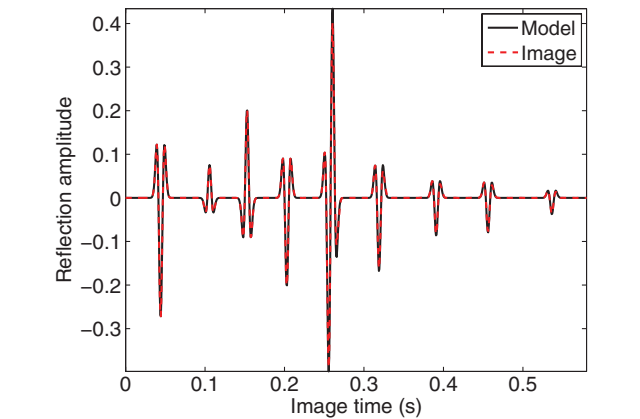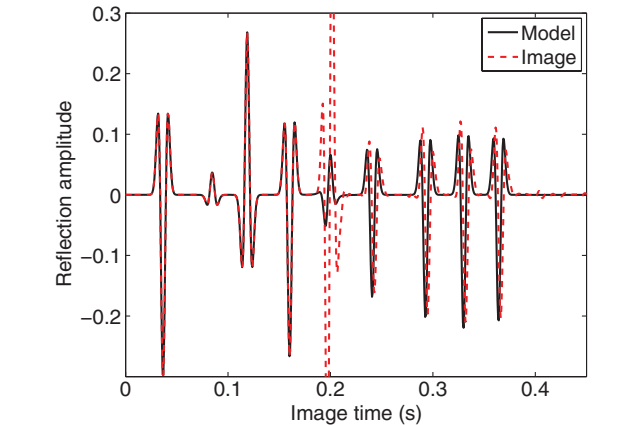

Figure 10. Image for 35° incidence angle.

fast thin layer and all waves below this thin layer propagate again. As it can be seen from the amplitude mismatch at 0.2 s, inside the thin layer the imaging scheme does not give the correct amplitude because waves that are evanescent at the imaging level are not properly treated by equation 25. For depth levels below the thin layer, the remaining four interfaces can still be imaged. Because tunneling waves show a phase shift due to the fact that the reflection coefficients of the top and bottom interfaces of the tunneling layer are complex, the image times and amplitudes are incorrect. If we look again at interface eight, the obtained reflection coefficient has an amplitude error of 3% and a timing error of 2.5 ms. This result can be improved by using a more accurate initial estimate and solve equations 29 and 30. We then compute the up- and downgoing Green's functions and create the image by deconvolution using equation 32. We show results of this approach below.

Imaging by MDD using equation 32

To correctly image inside and below thin layers, it can be necessary to include some multiples in the initial estimate of $\mathcal{T}_d$ because
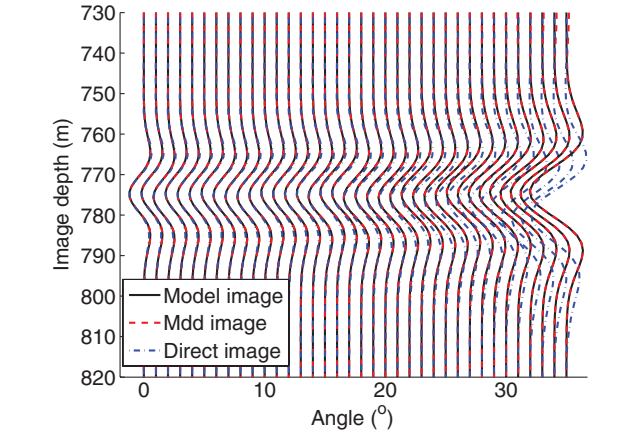

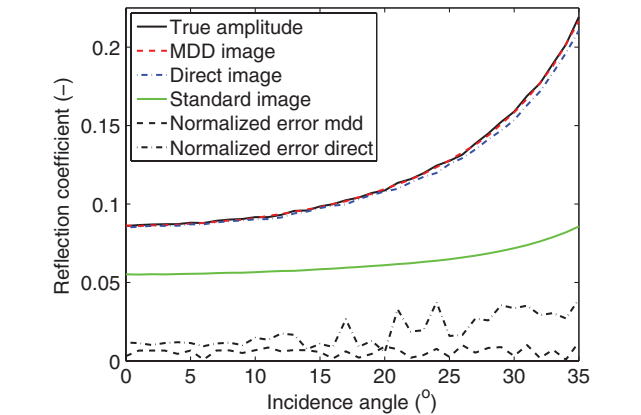Figure 11. Depth image of the eighth interface as a function of incidence angle.

Figure 12. Reflection coefficient amplitude from the direct imaging method and the MDD method of the eighth interface as a function of incidence angle.

this signal is not updated by the Marchenko-type scheme. Incorporating a good estimate of $\mathcal{T}_d$ in the scheme also allows for imaging interfaces below layers through which the waves have tunneled. To show the improvement of incorporating multiples in thin layers and the effect of tunneling, we take a close look at the eighth interface, which is located 776 m below the source. We select incidence angle dependent focus times at half the intercept times in the middle of the eighth layer. For this particular focus time, we compute the first arrival of the transmission event within the time window of the Ricker wavelet around the focus time. When the model is unknown, a smooth background model can be constructed in the same way as it is normally done for migration. This background model can then be used to generate the initial estimate. With this initial estimate, we solve equations 29 and 30, and compute the directional Green's functions of the angle-dependent equivalents of equations 13 and 14. From those, we construct the reflection response of the medium below the focus time with the aid of equation 32 and compute the time image by inverse wavefield extrapolation. We converted focus time to depth for display purposes. The result is given in Figure 11, which shows the angle-dependent local reflection coefficient image as a function of angle versus depth for the two imaging schemes. The red dashed lines are the image events obtained by starting with the correct first arrival followed by MDD and imaging. The blue dash-dotted lines are taken from the direct image of Figure 8 converted to depth. The black lines are obtained from modeling the expected primary event with the amplitude of the local reflection coefficient. Notice that the timing errors (displayed as depth errors) in the direct image result start to be visible around 25° where the wavelength at 40 Hz is almost nine times the thickness of the thin layer. For all angles of incidence, the thin layer effect has disappeared when the correct first arrival is used in combination with MDD. The reflection coefficient amplitude as a function of angle is shown in Figure 12 for the maximum amplitudes obtained from the time images that are displayed as depth images in Figure 11. The black dashed and dash-dotted lines give the normalized errors of the two numerical results shown in the dashed red and dash-dotted blue lines, respectively. The direct image, obtained with a scaled delta-function, is also very accurate for small angle of incidence. The error increases for angles larger than 20° due to neglecting the effect of the thin layer on the finite resolution result in solving the Marchenko-type equations. Still, the image amplitude errors remain well below 5%, whereas the deconvolution image shows errors around 1%. For comparison, the additional green solid line shows the amplitude obtained by standard one-way migration using the correct background velocity model. The large difference with the true values is caused by transmission and internal multiple effects.

DISCUSSION

The direct image is obtained by using a delta-function as initial estimate for the transmitted first arrival at the focus time. This has the advantage that the time-image can be formed without any knowledge of the subsurface. It has the disadvantage that thin layer effects and the effects of waves that tunnel above the image depth are not always properly accounted for. This can create small amplitude errors in the images of interfaces below thin layers, but it can create substantial time-errors when the waves have tunneled through a thin layer above the image depth. This is not a particular drawback of the method because no imaging scheme based on one-way propagation handles evanescent waves properly. In principle,

the constructed time image can be converted to depth by an inversion step that would compute the density and velocity from the obtained reflection coefficients as a function of incidence angle. In practice, this inversion can be quite difficult because it is a nonlinear process. Once the velocity of each layer is known, time-to-depth conversion can be performed to construct the final depth image.

The construction of an accurate estimate of the direct transmission event at the focus time can be necessary for obtaining an image that is better than the image obtained with a delta-function as first arrival. This can be done in the same way that is used in standard migration schemes by estimating a background model and use that to compute the first arrival of the transmission response. The importance of retrieving the Green's functions is twofold. First, the retrieved Green's functions are the downward continued wavefields from the measurement surface to the interior. These are retrieved from the measured reflection response without any modeling. Second, because the theory gives the upgoing and downgoing Green's function in the interior, one can immediately use these for imaging. This can be achieved by multidimensional deconvolution (van der Neut et al., 2011).

This is just a first step toward a new scheme for acoustic data imaging and possibly inversion. The present scheme is formulated in the intercept time-slowness domain, but it could have been formulated in space-time domain. The product of the reflection response and the upgoing and downgoing focusing functions as a function of slowness would become 2D convolutions in space over the horizontal coordinates of the receiver plane. The time instant of the direct arrival would become a function of each point on the receiver plane to the focusing point in the subsurface. We would lose the advantage of being able to solve for the focusing functions per slowness value, and for that reason we choose this option here.

Several open questions remain for further study, such as the effect of inaccuracies in the determined source wavelet, in the initial estimate, the effect of noise in the recorded data, and the effect of intrinsic losses in the earth. It is also important that this method can be generalized to 3D by combining the 3D method presented in Wapenaar et al. (2013a) and this scheme. This is not difficult in theory, but it will also present new challenges that are beyond the scope of the present study. We did see that the results are not exact when the image depth is at locations where the waves did not propagate and this will occur in a 3D settting in a more complicated way than in a 1D model. A second aspect is that a direct arrival time must be estimated for every receiver point on the surface to the focusing point, putting more conditions on the background model and complications may occur in strongly lateral heterogeneous models. This does not necessarily require more work than is done to build a background model for standard migration. Computing the total focusing wavefield from a similar Marchenko equation has been shown to work with computed 2D acoustic data (van der Neut et al., 2013; Wapenaar et al., 2013b).

CONCLUSIONS

We present an algorithm to compute the up- and downgoing parts of a focusing wavefield from the measured reflection response. This is done under the assumption of a plane wavefield and a 1D earth model. The focusing wavefield is then used together with the measured reflection response to compute the up- and downgoing VSP Green's functions representations. These two relations can be derived from the reciprocity theorems of the time-convolution and

Slob et al.

time-correlation types. The focusing wavefield focuses at the depth where the VSP Green's function has its virtual source. The up- and downgoing focusing wavefields are nonzero in a finite time window where the Green's functions are zero. Therefore, the focusing wavefields can be obtained from the reflection response by solving the resulting two coupled Marchenko-type equations.

We have shown that the downgoing focusing wavefield in the upper half space is the inverse of the transmission response. The upgoing focusing wavefield is the reflection response to the downgoing wavefield in a model that is the same as the earth from the surface to the focus depth, but is homogeneous below this focus depth. Once the two focusing wavefields are found from finite frequency bandwidth reflection data, a virtual VSP Green's function can be computed. We have shown that a subsurface image free from effects of multiple reflections in the data can be found directly in the upgoing part of the focusing wavefield or from performing multidimensional deconvolution on the VSP Green's functions.

The direct imaging method produces an image with accurate amplitudes, but small timing errors can occur for reflectors below a thin layer. In our example, this occurred when the layer thickness is less than one-eighth of the dominant wave length or when waves have tunneled through the thin layer. In that case, an improved initial estimate leads to a correct image using the MDD method.

APPENDIX A

WAVEFIELD FOCUSING AND GREEN'S FUNCTION REPRESENTATIONS

Wavefields in a medium with three interfaces

Let us look at the expressions for the reflection response $R(z_0, t)$ for a source and receiver at z_0 and the transmission response $T^+(z_2, z_0, t)$ for a source at z_0 and a receiver at z_2. In the frequency domain, the corresponding reflection $\hat{R}(z_0, \omega)$ and transmission $\hat{T}^+(z_2, z_0, \omega)$ responses generated by the unit amplitude plane wave are given by (Goupillaud, 1961)

$$\hat{R}(z_0, \omega) = \frac{r_0 + r_1 e^{-2i\omega t_1} + r_2 e^{-2i\omega(t_1+t_2)} + r_0 r_1 r_2 e^{-2i\omega t_2}}{1 + r_0 r_1 e^{-2i\omega t_1} + r_0 r_2 e^{-2i\omega(t_1+t_2)} + r_1 r_2 e^{-2i\omega t_2}},$$
(A-1)

$$\hat{T}^+(z_2, z_0, \omega)$$
$$= \frac{\tau_0^+ \tau_1^+ \tau_2^+ e^{-i\omega(t_1+t_2)}}{1 + r_0 r_1 e^{-2i\omega t_1} + r_0 r_2 e^{-2i\omega(t_1+t_2)} + r_1 r_2 e^{-2i\omega t_2}}, \quad \text{(A-2)}$$

where we notice that the denominators are the same for the reflection and transmission responses. Comparing the events in the reflection response shown in Figure A-1 with the numerator of the reflection response of equation A-1 we can see that they are the same. We conclude that sending in the inverse of the transmission response of equation A-2 is exactly the necessary wavefield that focuses to a unit amplitude at z_2 and in the time domain at $t = 0$. In the frequency domain, the focusing wavefield is therefore given by

$$\hat{f}_1^+(z_0, z_2, \omega) = \frac{1}{\hat{T}^+(z_0, z_2, \omega)} = e^{i\omega(t_1+t_2)}$$
$$\times \frac{1 + r_0 r_1 e^{-2i\omega t_1} + r_1 r_2 e^{-2i\omega t_2} + r_0 r_2 e^{-2i\omega(t_1+t_2)}}{\tau_0^+ \tau_1^+ \tau_2^+},$$
(A-3)

$$\hat{f}_1^-(z_0, z_2, \omega) = \frac{\hat{R}^+(z_0, \omega)}{\hat{T}^+(z_0, z_2, \omega)} = e^{i\omega(t_1+t_2)}$$
$$\times \frac{r_0 + r_1 e^{-2i\omega t_1} + r_0 r_1 r_2 e^{-2i\omega t_2} + r_2 e^{-2i\omega(t_1+t_2)}}{\tau_0^+ \tau_1^+ \tau_2^+}.$$
(A-4)

The four incident and four reflected wavefields are indicated in Figure A-1.

Derivation of the Green's function representations

Equation 10 can be derived from the reciprocity theorem of the time-convolution type and equation 11 can be obtained from the reciprocity theorem of the time-correlation type. For more information about acoustic reciprocity theorems, see de Hoop (1995). In 1D space and for a source free domain that is bounded by two depth levels, z_0 and z_i, they are given in the frequency domain by

$$\hat{p}_A(z_0, \omega)\hat{v}_{z,B}(z_0, \omega) - \hat{p}_B(z_0, \omega)\hat{v}_{z,A}(z_0, \omega)$$
$$= \hat{p}_A(z_i, \omega)\hat{v}_{z,B}(z_i, \omega) - \hat{p}_B(z_i, \omega)\hat{v}_{z,A}(z_i, \omega), \quad \text{(A-5)}$$

$$\hat{p}_A^*(z_0, \omega)\hat{v}_{z,B}(z_0, \omega) + \hat{p}_B(z_0, \omega)\hat{v}_{z,A}^*(z_0, \omega)$$
$$= \hat{p}_A^*(z_i, \omega)\hat{v}_{z,B}(z_i, \omega) + \hat{p}_B(z_i, \omega)\hat{v}_{z,A}^*(z_i, \omega), \quad \text{(A-6)}$$

where the subscripts A and B refer to two independent states and $\hat{v}_z(z, \omega)$ denotes the particle velocity related to pressure as
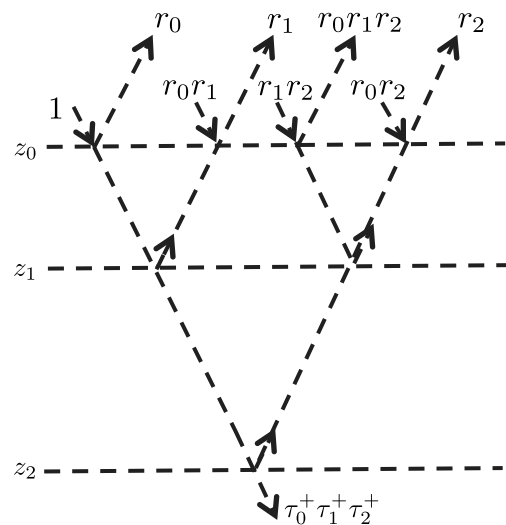

Figure A-1. The focusing wavefield incident on a medium with three interfaces consists of four events and the corresponding reflection response contains the same number of events at the same times; the wavefield focuses at the bottom interface.

$\hat{v}_z(z, \omega) = -(i\omega\rho(z))^{-1}\partial_z\hat{p}(z, \omega)$. We have assumed that no sources are present for $z_0 \leq z \leq z_i$ and that the media between the two levels are identical in the two states. Equation A-5 is generally valid under these assumptions, whereas equation A-6 is a correct equation under the additional assumption that the medium between the two depth levels is dissipation free. The pressure is the sum of down- and upgoing wavefields as $\hat{p}(z, \omega) = \hat{p}^+(z, \omega) + \hat{p}^-(z, \omega)$ and the particle velocity can be written as $\hat{v}_z(z, \omega) = -(i\omega\rho(z))^{-1}\partial_z[\hat{p}^+(z, \omega) + \hat{p}^-(z, \omega)]$. Substituting these decompositions in equations A-5 and A-6 and following a similar analysis as in Wapenaar and Berkhout (1989) gives

$$\rho_0^{-1} \lim_{z\uparrow z_0}(\hat{p}_A^+(z)\partial_z\hat{p}_B^-(z) + \hat{p}_A^-(z_0)\partial_z\hat{p}_B^+(z))$$
$$= -\rho_{i+1}^{-1} \lim_{z\downarrow z_i}(\hat{p}_B^-(z)\partial_z\hat{p}_A^+(z) + \hat{p}_B^-(z_i)\partial_z\hat{p}_A^-(z)), \quad \text{(A-7)}$$

$$\rho_0^{-1} \lim_{z\uparrow z_0}([\hat{p}_A^+(z)]^*\partial_z\hat{p}_B^+(z) + [\hat{p}_A^-(z)]^*\partial_z\hat{p}_B^-(z))$$
$$= -\rho_{i+1}^{-1} \lim_{z\downarrow z_i}(\hat{p}_B^+(z)[\partial_z\hat{p}_A^+(z)]^* + \hat{p}_B^-(z)[\partial_z\hat{p}_A^-(z)]^*), \quad \text{(A-8)}$$

where we have omitted ω in the arguments for brevity. We use equations A-5 and A-6 to a configuration in which state A corresponds to the medium that is homogeneous below z_i, whereas state B is the actual medium. In state A, we use the functions $\hat{f}_1^{\pm}$ that focus just below depth level z_i. Below the depth level z_i, the focusing wavefield is a unit amplitude downgoing wave that can be written as $f_1^+(z, z_i, \omega) = \exp[-i\omega(z - z_i)/c_{i+1}]$; because there is no upgoing wave, we have $f_1^-(z, z_i, \omega) = 0$. We then find

$$\hat{p}_A^{\pm}(z_0, \omega) = \hat{f}_1^{\pm}(z_0, z_i, \omega), \qquad \text{(A-9)}$$

$$\lim_{z\downarrow z_i}\partial_z\hat{p}_A^+(z, \omega) = -i\omega/c_{i+1}, \qquad \lim_{z\downarrow z_i}\partial_z\hat{p}_A^-(z, \omega) = 0. \qquad \text{(A-10)}$$

In state B, we take the actual configuration with a unit amplitude incident wave above the depth level z_0 given by $\hat{p}_B^+(z, \omega) = \exp[-i\omega(z - z_0)/c_0]$ and the reflection response is given by $\hat{p}_B^-(z, \omega) = \hat{R}(z_0, \omega)\exp[i\omega(z - z_0)/c_0]$. We find

$$\lim_{z\uparrow z_0}\partial_z\hat{p}_B^+(z, \omega) = -i\omega/c_0, \qquad \text{(A-11)}$$

$$\lim_{z\uparrow z_0}\partial_z\hat{p}_B^-(z, \omega) = i\omega\hat{R}(z_0, \omega)/c_0, \qquad \text{(A-12)}$$

$$\hat{p}_B^{\pm}(z_i, \omega) = \hat{G}^{\pm,q}(z_i, z_0, \omega), \qquad \text{(A-13)}$$

where just below depth level z_i, the wavefield is given by the up- and downgoing field Green's functions. Notice that, here, the sign in the superscript of the Green's function relates to upgoing and downgoing waves just below the level z_i, which is the receiver level for this Green's function. The superscript q indicates the wavefield is generated by a monopole source just above z_0. Substituting these choices in equation A-7 and A-8 leads to

$$\frac{Z_0}{Z_{i+1}}\hat{G}^{-,q}(z_i, z_0, \omega)$$
$$= \hat{R}(z_0, \omega)\hat{f}_1^+(z_0, z_i, \omega) - \hat{f}_1^-(z_0, z_i, \omega), \qquad \text{(A-14)}$$

$$\frac{Z_0}{Z_{i+1}}\hat{G}^{+,q}(z_i, z_0, \omega)$$
$$= [\hat{f}_1^+(z_0, z_i, \omega)]^* - \hat{R}(z_0, \omega)[\hat{f}_1^-(z_0, z_i, \omega)]^*, \quad \text{(A-15)}$$

where the impedance is given by $Z_i = \rho_ic_i$. Equations A-14 and A-15 are the wavefield retrieval equations for the scaled up- and downgoing wavefields, respectively, at the receiver level z_i that is obtained from the measured reflection response and the functions $\hat{f}_1^{\pm}$. Equation A-14 is equal to equation 10 and equation A-15 is equal to equation 11 because the Green's functions satisfy the reciprocity relation

$$Z_0\hat{G}^{\mp,q}(z_i, z_0, \omega) = Z_{i+1}\hat{G}^{p,\pm}(z_0, z_i, \omega), \qquad \text{(A-16)}$$

where $G^{p,\pm}(z_0, z_i, \omega)$ are the Green's functions of equations 10 and 11. The reason for the factors Z_0 and Z_{i+1} is that the Green's functions and the focusing functions have been defined according to the transmission responses and the downgoing and upgoing pressure transmission responses satisfy $Z_0\hat{T}^+(z_i, z_0, \omega) = Z_{i+1}\hat{T}^-(z_0, z_i, \omega)$. By adding equations A-14 and A-15 and using reciprocity of equation A-16, we find an expression for the Green's function corresponding to the virtual VSP as

$$\hat{G}(z_0, z_i, \omega) - [\hat{f}_2(z_i, z_0, \omega)]^* = \hat{R}(z_0, \omega)\hat{f}_2(z_i, z_0, \omega). \qquad \text{(A-17)}$$

Equation A-17 is the 1D equivalent of equation 9 in Wapenaar et al. (2013a) with $\hat{f}_2 = \hat{f}_2^- + \hat{f}_2^+ = \hat{f}_1^+ - [\hat{f}_1^-]^*$. Without going into the details of this relation, the equation shows that if we send in the focusing wavefield $f_2(z_i, z_0, t)$ the response is equal to the difference of the time-reverse of this function $f_2(z_i, z_0, -t)$ and the VSP Green's function.

Plane waves at oblique angles of incidence can be obtained by transforming the wavefields from space-time domain to the intercept-time slowness domain and the radial slowness p becomes a parameter. For each slowness value, equation A-7 remains valid and therefore also equation A-14 remains valid. Equation A-8 and therefore equation A-15 remain valid under the condition that the waves propagate through the depth levels z_0 and z_i, whereas they can be evanescent at depth levels between z_0 and z_i.

From this result, it would be a small step to deriving space-time relations for media with 3D variations in velocity and density, but this is beyond the scope of the current paper. Examples of such schemes and results on data modeled for 2D heterogeneous subsurface models can be found in Wapenaar et al. (personal communication, 2014) and Broggini et al. (personal communication, 2014).

REFERENCES

Agranovich, Z. S., and V. A. Marchenko, 1963, The inverse problem of scattering theory: Gordon and Breach.

Broggini, F., and R. Snieder, 2012, Connection of scattering principles: A visual and mathematical tour: European Journal of Physics, **33**, 593–613, doi: 10.1088/0143-0807/33/3/593.

Broggini, F., R. Snieder, and K. Wapenaar, 2012, Focusing the wavefield inside an unknown 1D medium: Beyond seismic interferometry: Geophysics, **77**, no. 5, A25–A28, doi: 10.1190/geo2012-0060.1.

Burridge, R., 1980, The Gelfand-Levitan, the Marchenko, and the Gopinath-Sondhi integral equations of inverse scattering theory, regarded in the context of inverse impulse response problems: Wave Motion, **2**, 305–323, doi: 10.1016/0165-2125(80)90011-6.

Coen, S., 1981, The inverse problem of the shear modulus and density profiles of a layered earth: Journal of Geophysical Research, **86**, 6052–6056, doi: 10.1029/JB086iB07p06052.

de Hoop, A. T., 1995, Handbook of radiation and scattering of waves: Academic Press.

Goupillaud, P. L., 1961, An approach to inverse filtering of near surface effects from seismic records: Geophysics, **26**, 754–760, doi: 10.1190/1.1438951.

Jakubowicz, H., 1998, Wave equation prediction and removal of interbed multiples: 68th Annual International Meeting, SEG, Expanded Abstracts, 1527–1530.

Lamb, G. L., 1980, Elements of Soliton theory: John Wiley & Sons Inc.

Newton, R. G., 1981, Inversion of reflection data for layered media: A review of exact methods: Geophysical Journal of the Royal Astronomical Society, **65**, 191–215, doi: 10.1111/j.1365-246X.1981.tb02708.x.

Raz, S., 1981, Direct reconstruction of velocity and density profiles from scattered field data: Geophysics, **46**, 832–836, doi: 10.1190/1.1441220.

Rose, J. H., 2002, Single-sided autofocusing of sound in layered materials: Inverse Problems, **18**, 1923–1934, doi: 10.1088/0266-5611/18/6/329.

ten Kroode, F., 2002, Prediction of internal multiples: Wave Motion, **35**, 315–338, doi: 10.1016/S0165-2125(01)00109-3.

van Dedem, E. J., and D. J. Verschuur, 2005, 3D surface-related multiple prediction: A sparse inversion approach: Geophysics, **70**, V31–V43, doi: 10.1190/1.1925752.

van der Neut, J., E. Slob, K. Wapenaar, J. Thorbecke, R. Snieder, F. Broggini, J. Behura, and S. Singh, 2013, Interferometric redatuming of autofocused primaries and internal multiples: 83rd Annual International Meeting, SEG, Expanded Abstracts, 4589–4594.

van der Neut, J., J. Thorbecke, K. Mehta, E. Slob, and K. Wapenaar, 2011, Controlled-source interferometric redatuming by crosscorrelation and multidimensional deconvolution in elastic media: Geophysics, **76**, no. 4, SA63–SA76, doi: 10.1190/1.3580633.

Verschuur, D. J., A. J. Berkhout, and C. P. A. Wapenaar, 1992, Adaptive surface-related multiple elimination: Geophysics, **57**, 1166–1177, doi: 10.1190/1.1443330.

Wapenaar, C. P. A., and A. J. Berkhout, 1989, Elastic wave field extrapolation: Redatuming of single- and multi-component seismic data: Elsevier Science Publishers, Advances in exploration geophysics.

Wapenaar, K., F. Broggini, E. Slob, and R. Snieder, 2013a, Three-dimensional single-sided Marchenko inverse scattering, data-driven focusing, Green's function retrieval, and their mutual relations: Physical Review Letters, **110**, 084301, doi: 10.1103/PhysRevLett.110.084301.

Wapenaar, K., F. Broggini, and R. Snieder, 2012, Creating a virtual source inside a medium from reflection data: Heuristic derivation and stationary-phase analysis: Geophysical Journal International, **190**, 1020–1024, doi: 10.1111/j.1365-246X.2012.05551.x.

Wapenaar, K., E. Slob, J. van der Neut, J. Thorbecke, F. Broggini, and R. Snieder, 2013b, Three-dimensional Marchenko equation for Green's function retrieval "beyond seismic interferometry": 83rd Annual International Meeting, SEG, Expanded Abstracts, 4573–4578.

Ware, J. A., and K. Aki, 1969, Continuous and discrete inverse-scattering problems in a stratified elastic medium. I. Plane waves at normal incidence: Journal of the Acoustical Society of America, **45**, 911–921, doi: 10.1121/1.1911568.

Weglein, A. B., F. Liu, X. Li, P. Terenghi, E. Kragh, J. D. Mayhan, Z. Wang, J. Mispel, L. Amundsen, H. Liang, L. Tang, and S.-Y. Hsu, 2012, Inverse scattering series direct depth imaging without the velocity model: First field data examples: Journal of Seismic Exploration, **21**, 1–28.

Zhang, H., and A. B. Weglein, 2009, Direct nonlinear inversion of multiparameter 1D elastic media using the inverse scattering series: Geophysics, **74**, no. 6, WCD15–WCD27, doi: 10.1190/1.3256283.